Rare Met. (2024) 43(1):389–394
https://doi.org/10.1007/s12598-023-02355-4

RARE METALS

LETTER

Observation of ballistic-diffusive thermal transport in GaN transistors using thermoreflectance thermal imaging

Zhi-Ke Liu, Yang Shen, Han-Ling Li, Bing-Yang Cao*

Received: 28 November 2022 / Revised: 16 January 2023 / Accepted: 8 February 2023 / Published online: 7 November 2023

To develop effective thermal management strategies for gallium-nitride (GaN) transistors, it is essential to accurately predict the device junction temperature. Since the width of the heat generation in the devices is comparable to phonon mean free paths (MFPs) of GaN, phonon ballistic transport exists and can significantly affect the heat transport process, which necessitates a thorough understanding of the influence of the phonon ballistic effects in GaN transistors. In this study, the ballistic-diffusive phonon transport in GaN-on-SiC devices is examined by measuring the hotspot temperature using the thermoreflectance thermal imaging (TTI) combined with the hybrid phonon Monte Carlo-diffusion simulations. A series of Au heaters are fabricated on the top of the GaN layer to quantitatively mimic the different heat source distributions during device operation. The experimental and simulation results show a good consistency and both indicate that the phonon ballistic effects can significantly increase the hotspot temperature. With the size of the heat source decreasing, the errors of Fourier's law-based predictions increase, which emphasizes the necessity to carefully consider the phonon ballistic transport in device thermal simulations.

GaN high electron mobility transistors (HEMTs) are attractive devices for high-voltage and high-frequency applications due to their high breakdown voltage and high electron mobility [1, 2]. However, owing to the high power density (> 40 W mm^{-1}) [3], GaN HEMTs hold very high junction temperatures [4] which leads to a severe thermal concern [5]. It has been demonstrated that a 10 °C increase in the junction temperature can make the reliability of electronic devices decrease by 50% [6, 7]. An accurate assessment of the junction temperature of GaN HEMTs is critical to predict the device lifetime and develop effective thermal management strategies [8].

In GaN HEMTs, most heat is generated on the top of the GaN layer and concentrated at the drain-side gate edge [9, 10] with a width of a few hundred nanometers. The characteristic size is comparable to MFPs of phonons, which are the dominant heat carriers in GaN [11, 12]. Owing to the lack of phonon scattering in the heat source region, Fourier's law of heat conduction becomes inapplicable and significantly underestimates the hotspot temperature [13–15]. Also, being the result of Joule heating, the heat generation in GaN HEMTs is highly bias-dependent, i.e., the heat source distributions can be quite different under different working conditions. To accurately predict the junction temperature, it is essential to clearly understand the heat source size dependence of phonon ballistic effects, and their influence on the temperature.

Experimental efforts have been made to study the heat source size-induced phonon ballistic transport, including the studies using pulsed/modulated laser thermoreflectance [16], ultrafast coherent soft X-rays diffraction [14], transient thermal grating [17], extreme ultraviolet thermal and acoustic nanometrology [18], etc. However, in these techniques, only the strength of the phonon ballistic effect can be inferred indirectly, the hotspot temperature and the device temperature field cannot be measured, which partly restrict the applications of these results in real devices [19]. As a non-contact optical technique, TTI can directly detect the surface temperature with a submicron spatial resolution

Supplementary Information The online version contains supplementary material available at https://doi.org/10.1007/s12598-023-02355-4.

Z.-K. Liu, Y. Shen, H.-L. Li, B.-Y. Cao*
Key Laboratory for Thermal Science and Power Engineering of Ministry of Education, Department of Engineering Mechanics, Tsinghua University, Beijing 100084, China
e-mail: caoby@tsinghua.edu.cn

[20–25]. Compared with the above-mentioned methods, the influence of the phonon ballistic transport on the hotspot temperature can be directly detected by TTI, which can provide a more intuitive understanding of the phonon ballistic transport in real devices [26–28].

In this work, the influence of the phonon ballistic transport on the hotspot temperature in GaN HEMTs was studied using TTI. A series of Au heaters with different widths were fabricated on the top of the GaN layer to quantitatively mimic the different heat source distributions in GaN HEMTs. The temperature fields and the hotspot temperatures of different samples were directly measured by TTI. Hybrid Monte Carlo (MC)-diffusion simulations were also conducted to validate the experimental results. Both the experimental and simulation results indicate that with the decrease in the heat source size, the hotspot temperature is much higher than the Fourier's law-based predictions. It is emphasized that the phonon ballistic effects should be carefully considered to accurately predict the device junction temperature.

TTI is an experimental technique to measure the surface temperature field with a high spatial resolution up to hundreds of nanometers. The spatial resolution can reach 353 nm by a 530-m light source and a 100 × objective lens with a numerical aperture of 0.75, which makes TTI a highly effective technique to detect the hotspot temperature in electronic devices. TTI deduces the temperature field by probing the variation of the surface reflectivity with respect to temperatures. Under common working conditions of electronic devices, the dependence of the relative change in reflectivity on temperatures is linear, which can be expressed as:

$$\frac{\Delta r}{r} = \left(\frac{1}{r}\frac{\partial r}{\partial T}\right)\Delta T = C_{\mathrm{TR}}\Delta T, \quad (1)$$

where r and ΔT represent the reflectivity and the temperature rise of the material surface, respectively. C_{TR} is the coefficient of thermoreflectance [29], which is related to the type of material, the wavelength of light, and the surface roughness of the sample [30]. The range of C_{TR} is usually from 1×10^{-5} to 1×10^{-2} K^{-1} for common metals and semiconductors. In prior to measuring the device temperature, the values of C_{TR} of different samples are calibrated with adequate data averaging to improve the signal to noise ratio of the experiments [26].

TTI experiment system includes five subsystems, as shown in Fig. 1. During the experiment, the excitation subsystem produces an excitation signal, which is collected by the device under test (DUT), and then a constant light-emitting diode (LED) light is shined on the DUT. The incident light is irradiated to the DUT surface through the microscope subsystem, and the reflected light from the

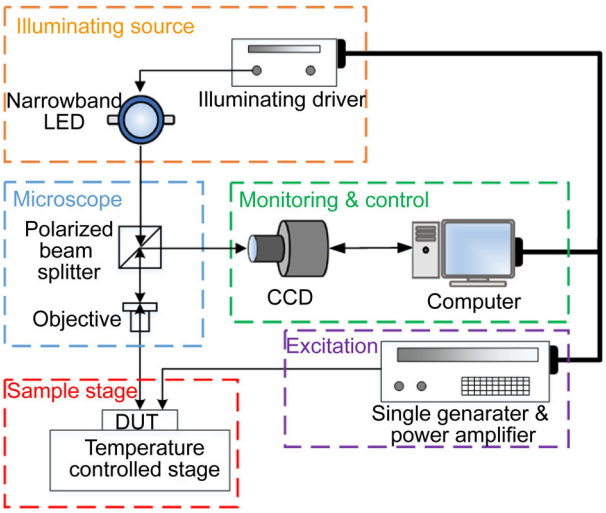

Fig. 1 Schematic diagram of thermoreflectance thermal imaging

DUT is captured by a charge coupled device (CCD) camera with synchronous lock-in detection. The excitation signals can lead to the temperature rise of the DUT surface, and then the changed light intensity with respect to the temperature changes can be detected by the CCD. The surface temperature distributions can be extracted from the variation of the light intensity and C_{TR} of the corresponding material. The timing setting of the excitation signal, the synchronous control of incident light, and the data analysis are completed by automatic system.

The structure of the samples being measured is shown in Fig. 2, which consists of four layers. From top to bottom, they are a 25-nm SiO_2 passivation layer, 2.1-μm GaN buffer layer, a 50-nm AlN nucleation layer, and a 350-μm SiC substrate. The width and the length of the sample are W = 7.5 mm and L = 7.5 mm, respectively. Au heaters were fabricated on the top of the samples through electron beam lithography, metallization, and lift-off process. The widths of the Au heaters (w_g) in different samples are 500 nm, 1, 2, 5, and 10 μm. For the convenience of electrical excitation and electrical measurement of the heater resistance with the four-wire method, four contact pads in the size of 300 μm × 300 μm were fabricated for each heater. As a supplement, the measurement results of resistance thermometer are analyzed and discussed in the Supporting Information. Figure 3a, b shows the sample surface taken by the CCD. The white area is a pair of heaters with four pads, and the gray part is the top surface of the GaN layer.

To measure the heat source temperatures of the samples, the 530 nm visible green LED light source was selected since it is sensitive to the temperature changes of Au [31, 32]. The coefficient of thermoreflectance C_{TR} was

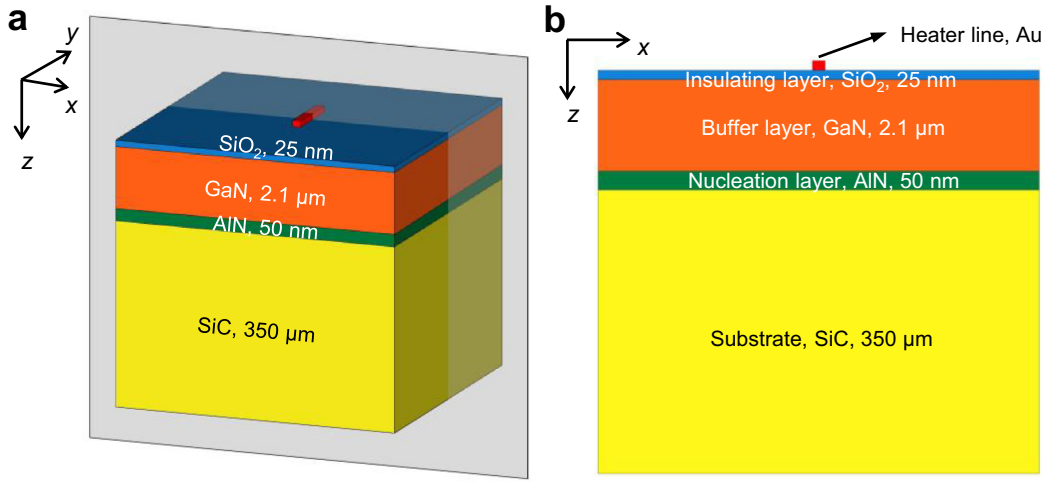

Fig. 2 Sample structure diagram of **a** three-dimensional structure and **b** cross section

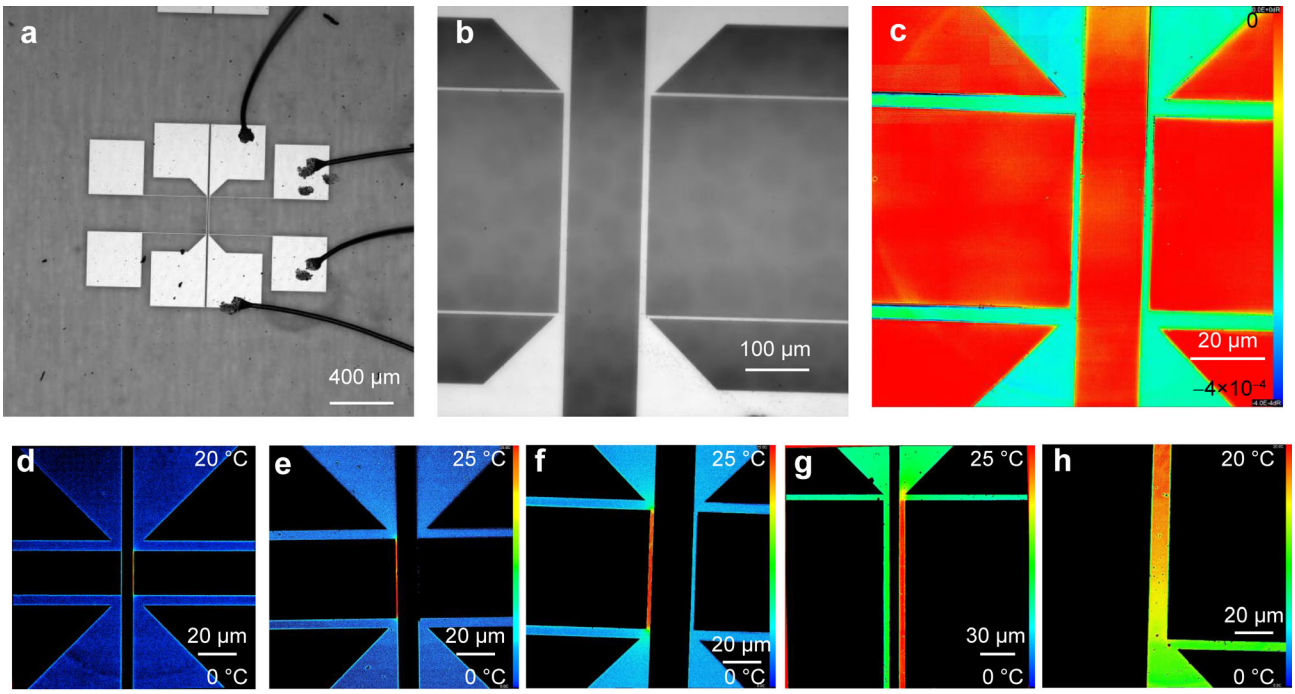

Fig. 3 Micrograph of upper surface of sample taken by CCD by **a** 5 × objective lens and **b** 20 × objective lens; **c** distributions of C_{TR} on surface of sample with w_g = 2 μm, in which green area represents Au material; two-dimensional maps of temperature rises in GaN samples heated by Au heaters with different w_g: **d** 500 nm, **e** 1 μm, **f** 2 μm, **g** 5 μm, and **h** 10 μm

determined by detecting the variation of the reflectivity with respect to a fixed 20 °C temperature difference applied to the samples, as indicated in Eq. (1). The measured C_{TR} of Au of different samples are all -2.8×10^{-4} K^{-1}. Figure 3c shows the C_{TR} distributions of the sample with w_g = 2 μm. It can be found that C_{TR} in the Au region is uniform and constant, which indicates the effectiveness of the measurements.

With the C_{TR} determined, the hotspot temperature rises of the samples with different power dissipations can be measured. The heating power was controlled by the input signal of the electrical excitation. Figure 3d–h shows the two-dimensional temperature rise distributions of the samples with different w_g. It can be found that the temperature rise mainly exists in the Au region and decays rapidly away from the heat source. Therefore, the average temperature rise in the Au region was defined as the hotspot temperature rise in this work. Figure 4a shows the hotspot temperature rise varying with the power dissipation of the sample with w_g = 5 μm. A good linear dependence

is achieved, and the fitted thermal resistance R_{TTI} is 75.52 K·W^{-1}. The experiments on other samples also show a similar linearity.

Figure 4b shows the measured thermal resistance R_{TTI} varying with w_g. The Fourier's law-based FEM-calculated thermal resistance R_{FEM} and the ratio between R_{TTI} and R_{FEM} are also given for comparison. The thermal conductivities of GaN and SiC were set as 168 [33] and 350 W·m^{-1}·K^{-1} [34], respectively. Additionally, the results obtained from the resistance thermometer R_{RT} are included and thoroughly discussed in the Supporting Information. As shown in Fig. 4b, R_{TTI}, R_{RT} and R_{FEM} increase rapidly with w_g decreasing, which can be attributed to the enhancement of the thermal spreading effect [35]. When heat spreads from a small source to a much larger region, there is a significant thermal spreading resistance, which increases with the decreased heat source size [36]. However, it can be noted that when w_g is small enough, i.e., $w_g < 1$ μm, R_{TTI} becomes larger than the FEM-based predictions, and the deviation is enlarged with the decrease in w_g. This indicates that with the decrease in the heat source size, the phonon ballistic effect is enhanced, which leads to a much higher junction temperature.

To illustrate the influence of the phonon ballistic effects on the thermal resistance more clearly, hybrid phonon MC-diffusion simulations are carried out for comparison with the experimental results [37, 38]. Considering the phonon ballistic effects mainly exist around the boundaries and the heat source, in the hybrid simulation, the total device is divided into three parts: (1) the top MC zone that covers the entire GaN layer and a region extending from the GaN/SiC interface; (2) the bottom MC zone that covers the bottom boundary; and (3) the middle diffusion zone. Phonon MC simulations [39] are conducted only in the MC zone, and FEM simulations are carried out in the diffusion zone. There is an overlap region between the MC zone and adjacent diffusion zone, which is used for the information transfer and convergence check. To couple the phonon tracing MC and Fourier's law of heat conduction, an alternating method, similar to the Schwarz technique proposed for the coupled Stokes/direct simulation MC problem in the fluidic simulation [40], is used in the overlap region. The basic idea of the method is to use the solution of the MC zone as the boundary condition of the diffusion zone in the next iteration, the solution of the diffusion zone as the boundary condition of the MC zone, and the overlap zone works as an indicator of the coupling effect. Here, an implicit temperature boundary condition is used for phonon MC in the hybrid method. Similar to the traditional given temperature boundary, all incident phonons are absorbed and subsequently re-emitted as phonons from a black-body boundary, following the boundary temperature T_{bnd}. The main difference is that T_{bnd} is determined in the traditional given temperature boundary, while T_{bnd} is unknown in the implicit temperature boundary condition, which needs to be determined by the iterative calculation of the diffusion solution.

The results of FEM based on Fourier's law (R_{FEM}) are used as reference values to calculate the thermal resistance ratio R/R_{FEM} obtained by TTI measurements and hybrid phonon MC-diffusion simulations, respectively, and Fig. 4c shows R/R_{FEM} varying with the heat source size. Some values extracted from the literatures are also given for comparison. The influence of the thermal spreading effect is eliminated in R/R_{FEM}; thus, the ratio can reflect the impact of the phonon ballistic effects on the device thermal resistance. In Fig. 4c, it can be found that R/R_{FEM} increases with the decreased w_g, which implies the enhancement of the phonon ballistic effects. In the near-junction heat transport process [37], two kinds of phonon ballistic effects

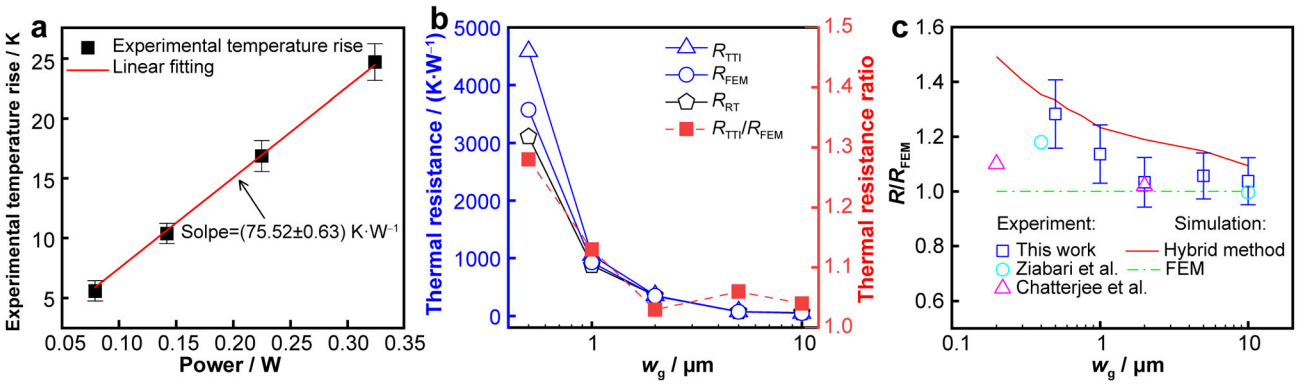

Fig. 4 **a** Linear dependence of hotspot temperature rise measured by TTI on power dissipation, where curve slope is device thermal resistance; **b** TTI and FEM results of thermal resistance varying with size of heaters, where thermal resistance ratio is defined as ratio between thermal resistance predicted by TTI and FEM, and it also includes the results from the resistance thermometer (R_{RT}); **c** experimental and simulated thermal resistance ratios varying with w_g, where reference values are extracted from Refs. [19, 41]

exist: one is the cross-plane ballistic effect caused by the phonon-boundary scattering, which is determined by the thickness of the GaN thin film. The other is the ballistic effect with the heat source size comparable to the phonon MFP. Since the thickness-dependent thermal conductivity of the GaN film is adopted in the FEM model, the deviation between R/R_{FEM} and 1 can reflect the influence of the heat source size-induced ballistic effect on the thermal transport process. The results indicate that the ballistic effect with the heat source size comparable with the MFP is significantly enhanced with the decreased heat source size. It is illustrated that only using thickness-dependent thermal conductivities in FEM simulations will underestimate the phonon ballistic effect, which can lead to a lower junction temperature. The underestimation can increase with the decrease in the heat source size, e.g., at a negative bias when the heat is highly concentrated at the drain-side gate edge in GaN HEMTs [41]. It is emphasized that a multiscale thermal simulation is essential to accurately predict the device junction temperature.

In summary, the temperature field of the GaN devices was measured by TTI. Au heaters with different widths were fabricated on the top of the GaN layer to mimic the different heat source distributions during device operation. The thermal resistance of the different samples is deduced by conducting experiments with a series of power dissipations. It is found that with the decrease in the heat source size, the measured thermal resistance becomes higher than Fourier's law-based predictions, which can be attributed to the phonon ballistic effects. Hybrid phonon MC-diffusion simulations are carried out to investigate the influence of the phonon ballistic transport. It is illustrated that with the decrease in the size of the heat source, the ballistic effect with the heat source size comparable with phonon MFP is significantly enhanced, which leads to a much higher hotspot temperature. The results emphasize the necessity of multiscale simulations and the need of high-resolution experiments to accurately predict the device junction temperature.

Acknowledgements This study was financially supported by the National Natural Science Foundation of China (Nos. 52327809, 51825601 and U20A20301).

Declarations

Conflict of interest The authors declare that they have no conflict of interest.

References

[1] Parker M. A gallium nitride HEMT that enhances. Nat Electron. 2021;4(12):858. https://doi.org/10.1038/s41928-021-00698-3.

[2] Lei C, Chen T, Yan B, Xiao XM. Reaction characteristics and kinetics of gallium in chlorination roasting of copper tailings using calcium chloride. Rare Met. 2022;41(3):1063. https://doi.org/10.1007/s12598-015-0499-0.

[3] Guggenheim R, Rodes L. Roadmap review for cooling high--power GaN HEMT devices. In: 2017 IEEE international conference on microwaves, antennas, communications and electronic systems (COMCAS). Tel-Aviv; 2017. https://doi.org/10.1109/COMCAS.2017.8244734.

[4] Liu JS, Li Y, Wang SW, Chen SF, Song HW, Zhang SH. Formation mechanism of local pits on surface of flattened sintered heat pipes. Chin J of Rare Met. 2022,46(5):597. https://doi.org/10.13373/j.cnki.cjrm.XY21020002.

[5] Wang SW, Song HW, Chen Y, Zhang SH, Hu KY, Zhu Y. Micro-mechanism and influencing factors of orange peel defects on bended surface of sintered pure copper heat pipe. Chin J of Rare Met. 2022,46(1):1. https://doi.org/10.13373/j.cnki.cjrm.XY20010023.

[6] Sohel Murshed SM, Nieto-De-Castro CA. A critical review of traditional and emerging techniques and fluids for electronics cooling. Renew Sustain Energy Rev. 2017;78:821. https://doi.org/10.1016/j.rser.2017.04.112.

[7] Zhang Y, Liu S. The optimization model of the heat conduction structure. Prog Nat Sci. 2008;18(6):665. https://doi.org/10.1016/j.pnsc.2008.01.010.

[8] Garimella SV, Persoons T, Weibel JA, Gektin V. Electronics thermal management in information and communications technologies: challenges and future directions. IEEE Trans Compon Packag Manuf Technol. 2017;7(8):1191. https://doi.org/10.1109/TCPMT.2016.2603600.

[9] Fletcher ASA, Nirmal D. A survey of gallium nitride HEMT for RF and high power applications. Superlattices Microstruct. 2017;109:519. https://doi.org/10.1016/j.spmi.2017.05.042.

[10] Sridharan S, Venkatachalam A, Yoder PD. Electrothermal analysis of AlGaN/GaN high electron mobility transistors. J Comput Electron. 2008;7(3):236. https://doi.org/10.1007/s10825-008-0210-x.

[11] Donmezer N, Graham S. The impact of noncontinuum thermal transport on the temperature of AlGaN/GaN HFETs. IEEE Trans Electron Devices. 2014;61(6):2041. https://doi.org/10.1109/TED.2014.2318672.

[12] Ma J, Wang X, Huang B, Luo X. Effects of point defects and dislocations on spectral phonon transport properties of wurtzite GaN. J Appl Phys. 2013;114(7):074311. https://doi.org/10.1063/1.4817083.

[13] Chen G. Ballistic-diffusive heat-conduction equations. Phys Rev Lett. 2001;86(11):2297. https://doi.org/10.1103/PhysRevLett.86.2297.

[14] Chen D, Jiang F, Fang L, Zhu YB, Ye CC, Liu WS. Machine learning assisted discovering of new M_2X_3-type thermoelectric materials. Rare Met. 2022;41(5):1543. https://doi.org/10.1007/s12598-021-01911-0.

[15] Chen G. Non-Fourier phonon heat conduction at the microscale and nanoscale. Nat Rev Phys. 2021;3:555. https://doi.org/10.1038/s42254-021-00334-1.

[16] Cahill DG. Analysis of heat flow in layered structures for time-domain thermoreflectance. Rev Sci Instrum. 2004;75(12):5119. https://doi.org/10.1063/1.1819431.

[17] Johnson JA, Maznev AA, Bulsara MT, Fitzgerald EA, Harman TC, Calawa S, Vineis CJ, Turner G, Nelson KA. Phase-controlled, heterodyne laser-induced transient grating measurements of thermal transport properties in opaque material. J Appl Phys. 2012;111(2):023503. https://doi.org/10.1063/1.3675467.

[18] Frazer TD, Knobloch JL, Hoogeboom-Pot KM, Nardi D, Chao W, Falcone RW, Murnane MM, Kapteyn HC,

Hernandez-Charpak JN. Engineering nanoscale thermal transport: size- and spacing-dependent cooling of nanostructures. Phys Rev Appl. 2019;11(2):024042. https://doi.org/10.1103/PhysRevApplied.11.024042.
[19] Ziabari A, Torres P, Vermeersch B, Xuan Y, Cartoixà X, Torelló A, Bahk J, Koh YR, Parsa M, Ye PD, Alvarez FX, Shakouri A. Full-field thermal imaging of quasiballistic crosstalk reduction in nanoscale devices. Nat Commun. 2018;9(1):255. https://doi.org/10.1038/s41467-017-02652-4.
[20] Farzaneh M, Maize K, Lüerßen D, Summers JA, Mayer PM, Raad PE, Pipe KP, Shakouri A, Ram RJ, Hudgings JA. CCD-based thermoreflectance microscopy: principles and applications. J Phys D Appl Phys. 2009;42(14):143001. https://doi.org/10.1088/0022-3727/42/14/143001.
[21] Hanus R, Rangnekar SV, Mollah S, Hussain K, Hines N, Heller E, Hersam MC, Khan A, Graham S. Thermoreflectance imaging of (ultra)wide band-gap devices with MoS_2 enhancement coatings. ACS Appl Mater Interfaces. 2021;13(35):42195. https://doi.org/10.1021/acsami.1c11528.
[22] Pavlidis G, Yates L, Kendig D, Lo C, Marchand H, Barabadi B, Graham S. Thermal performance of GaN/Si HEMTs using near-bandgap thermoreflectance imaging. IEEE Trans Electron Devices. 2020;67(3):822. https://doi.org/10.1109/TED.2020.2964408.
[23] Chatterjee B, Jayawardena A, Heller E, Snyder DW, Dhar S, Choi S. Thermal characterization of gallium oxide Schottky barrier diodes. Rev Sci Instrum. 2018;89(11):114903. https://doi.org/10.1063/1.5053621.
[24] de Freitas LR, da Silva EC, Mansanares AM, Tessier G, Fournier D. Sensitivity enhancement in thermoreflectance microscopy of semiconductor devices using suitable probe wavelengths. J Appl Phys. 2005;98(6):063508. https://doi.org/10.1063/1.2043231.
[25] Voigt P, Hartmann J, Reichling M. Thermal wave imaging of electrically heated microstructures. J Appl Phys. 1996;80(4):2013. https://doi.org/10.1063/1.363094.
[26] Vermeersch B, Bahk J, Christofferson J, Shakouri A. Thermoreflectance imaging of sub 100 ns pulsed cooling in high--speed thermoelectric microcoolers. J Appl Phys. 2013;113(10):104502. https://doi.org/10.1063/1.4794166.
[27] Batista JA, Mansanares AM, Da Silva EC, Vaz CC, Miranda LCM. Contrast enhancement in the detection of defects in transparent layered structures: the use of optothermal interference technique in solar cell investigation. J Appl Phys. 2000;88(9):5079. https://doi.org/10.1063/1.1312849.
[28] Martin-Horcajo S, Pomeroy JW, Lambert B, Jung H, Blanck H, Kuball M. Transient thermoreflectance for gate temperature assessment in pulse operated GaN-based HEMTs. IEEE Electron Device Lett. 2016;37(9):1197. https://doi.org/10.1109/LED.2016.2595400.
[29] Pierścińska D. Thermoreflectance spectroscopy-analysis of thermal processes in semiconductor lasers. J Phys D Appl Phys. 2017;51(1):13001. https://doi.org/10.1088/1361-6463/aa9812.
[30] Wang ZD, Lai ZQ. Preparation and characterization of single (200)-oriented TiN thin films deposited by DC magnetron reactive sputtering. Rare Met. 2022;41(4):1380. https://doi.org/10.1007/s12598-015-0517-2.
[31] Mayer PM, Lüerßen D, Ram RJ, Hudgings JA. Theoretical and experimental investigation of the thermal resolution and dynamic range of CCD-based thermoreflectance imaging. J Opt Soc Am A. 2007;24(4):1156. https://doi.org/10.1364/JOSAA.24.001156.
[32] Favaloro T, Bahk JH, Shakouri A. Characterization of the temperature dependence of the thermoreflectance coefficient for conductive thin films. Rev Sci Instrum. 2015;86(2):024903. https://doi.org/10.1063/1.4907354.
[33] Yang G, Cao B. Three-sensor 3ω–2ω method for the simultaneous measurement of thermal conductivity and thermal boundary resistance in film-on-substrate heterostructures. J Appl Phys. 2023;133(4):045104. https://doi.org/10.1063/5.0120284.
[34] Yuan C, Pomeroy JW, Kuball M. Above bandgap thermoreflectance for non-invasive thermal characterization of GaN--based wafers. Appl Phys Lett. 2018;113(10):102101. https://doi.org/10.1063/1.5040100.
[35] Razavi M, Muzychka YS, Kocabiyik S. Review of advances in thermal spreading resistance problems. J Thermophys Heat Transf. 2016;30(4):863. https://doi.org/10.2514/1.T4801.
[36] Hua YC, Li HL, Cao BY. Thermal spreading resistance in ballistic-diffusive regime for GaN HEMTs. IEEE Trans Electron Devices. 2019;66(8):3296. https://doi.org/10.1109/TED.2019.2922221.
[37] Li HL, Hua YC, Cao BY. A hybrid phonon Monte Carlo-diffusion method for ballistic-diffusive heat conduction in nano- and micro- structures. Int J Heat Mass Transf. 2018;127:1014. https://doi.org/10.1016/j.ijheatmasstransfer.2018.06.080.
[38] Li HL, Shen Y, Hua YC, Sobolev SL, Cao BY. Hybrid Monte Carlo-diffusion studies of modeling self-heating in ballistic-diffusive regime for gallium nitride HEMTs. J Electron Packag. 2022;145(1):011203. https://doi.org/10.1115/1.4054698.
[39] Hua YC, Cao BY. Phonon ballistic-diffusive heat conduction in silicon nanofilms by Monte Carlo simulations. Int J Heat Mass Transf. 2014;78:755. https://doi.org/10.1016/j.ijheatmasstransfer.2014.07.037.
[40] Aktas O, Aluru NR. A combined continuum/DSMC technique for multiscale analysis of microfluidic filters. Journal of Comput Phys. 2002;178(2):342. https://doi.org/10.1006/jcph.2002.7030.
[41] Chatterjee B, Dundar C, Beechem TE, Heller E, Kendig D, Kim H, Donmezer N, Choi S. Nanoscale electro-thermal interactions in AlGaN/GaN high electron mobility transistors. J Appl Phys. 2020;127(4):044502. https://doi.org/10.1063/1.5123726.